

Influence of Li Content on the Topological Inhibition of Oxygen Loss in Li-Rich Cathode Materials

Zhefeng Chen, Wentao Zhang, Jiajie Liu, Mingzheng Zhang, Shunning Li,* and Feng Pan*

Lithium-rich layer oxide cathodes are promising energy storage materials due to their high energy densities. However, the oxygen loss during cycling limits their practical applications. Here, the essential role of Li content on the topological inhibition of oxygen loss in lithium-rich cathode materials and the relationship between the migration network of oxygen ions and the transition metal (TM) component are revealed. Utilizing first-principles calculations in combination with percolation theory and Monte Carlo simulations, it is found that TM ions can effectively encage the oxidized oxygen species when the TM concentration in TM layer exceeds 5/6, which hinders the formation of a percolating oxygen migration network. This study demonstrates the significance of rational compositional design in lithium-rich cathodes for effectively suppressing irreversible oxygen release and enhancing cathode cycling performance.

1. Introduction

The development of clean and renewable energy sources is widely regarded as the key to reducing carbon emissions and diminishing reliance on fossil fuels. Lithium-ion batteries (LIBs), owing to their high energy density and environmentally friendly characteristics, have been extensively used in portable electronic devices.^[1–4] With the continuous popularity of electric vehicles and smart grids, the search is going on for the next-generation LIB cathodes that satisfy the requirement of lower cost, higher energy density, and better cycling stability. One well-known candidate is the family of Li-rich layered oxide (LRLO) cathodes, which can exhibit much higher energy density than contemporary counterparts and is generally composed of inexpensive transition metal (TM) elements such as Mn.^[5–9] However, current LRLOs still suffer from inferior cycling stability and poor rate capability, which constrains their practical application in the commercial market.

Li₂MnO₃, a typical material for the study of LRLO cathodes, is composed of Mn⁴⁺ cations that form a honeycomb structure

with Li located in the center of the Mn rings. The theoretical capacity of Li₂MnO₃ is 458mAh g⁻¹ if all Li are extracted from the lattice. As the Mn⁴⁺ ions in octahedral sites cannot be further oxidized to higher valence state, the redox of O²⁻ anions is triggered, leading to a voltage plateau of over 4.4 V. This anionic redox activity is demonstrated to be related with the Li–O–Li configuration in the lattice^[10–15] because the energy level of the unhybridized O 2*p* states is higher than that of the O 2*p* orbitals hybridized with Mn 3*d*. In comparison with Li₂MnO₃, the typical layered structure of LiMnO₂ cathode material corresponds to a theoretical capacity of 285mAh g⁻¹. The constituent Mn cations have a valency of +3 rather than +4, and Mn redox is thus expected instead of O redox upon Li

extraction. While in experiments the O3-structure LiMnO₂ is hardly synthesizable, it is interesting from a theoretical point of view to compare the intrinsic properties between Li₂MnO₃ and LiMnO₂, which may give insights into the degradation mechanism of LRLOs.

One of the most detrimental degradation mechanisms of LRLO cathode materials is the release of oxygen gas during cycling, which results in rapid capacity decay.^[16–22] To overcome this challenge, several recent works rely on the control of Li content in the lattice and design special layered stacking structures to effectively tune the distribution of Li–O–Li moieties.^[19,23–25] It is demonstrated that the oxidized O anions can be encaged in the lattice when their diffusivity to the surface is substantially reduced. These results encourage us to gain a better mechanistic understanding regarding the influence of Li content on the control of oxygen loss, as well as the concomitant TM migration phenomenon during the cycling of LRLO cathodes.

In this work, we use a combination of first principles calculations, Monte Carlo simulations, and percolation theory to evaluate the stability of O redox and the efficiency of TM migration upon Li extraction in a prototypical family of Li[Li_{1-x}Mn_x]O₂ cathode materials (Li₂MnO₃ corresponds to *x* = 2/3). As shown in **Figure 1**, five configurations of ordered structures with various Li content are constructed, from which we compare the thermodynamic stability of O anions in the lattice and the activation energy barrier of O migration. The kinetics of Mn ions are also evaluated, and a close link is discovered between the redistribution of Mn ions and the pathways for O migration. The percolation capability of redox-active O ions is obtained according to the Monte Carlo simulation results of the Li-rich samples, from which we

Z. Chen, W. Zhang, J. Liu, M. Zhang, S. Li, F. Pan
School of Advanced Materials
Peking University
Shenzhen Graduate School
Shenzhen 518055, P. R. China
E-mail: lism@pku.edu.cn; panfeng@pku.edu.cn

The ORCID identification number(s) for the author(s) of this article can be found under <https://doi.org/10.1002/adma.202403307>

DOI: 10.1002/adma.202403307

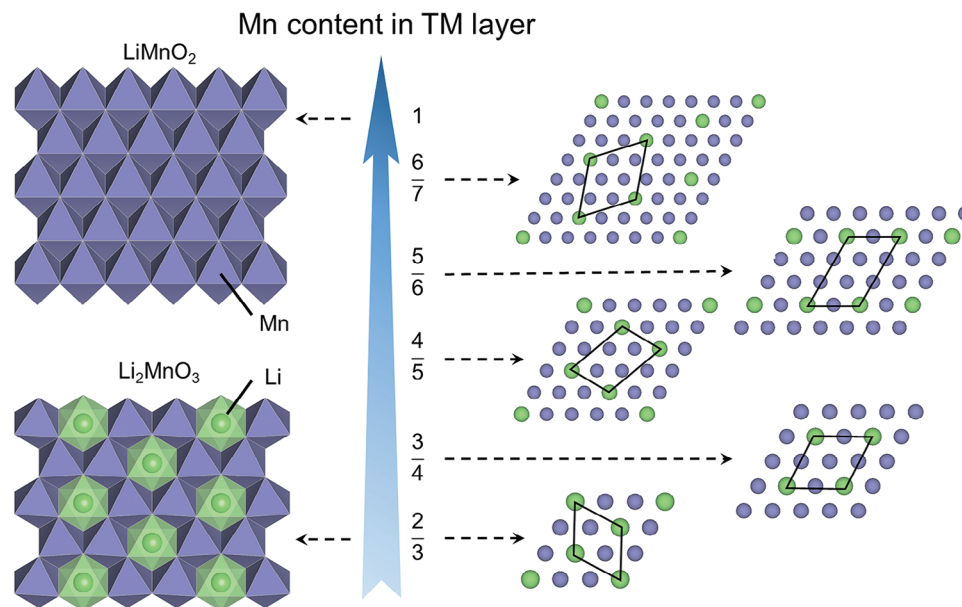


Figure 1. Typical ordered structures of $\text{Li}[\text{Li}_{1-x}\text{Mn}_x]\text{O}_2$ at $2/3 < x < 1$. Color code: Mn, blue; Li, green.

find a threshold value of $x = 5/6$ that determines the ability of O migration. Mn content higher than this threshold is revealed to be effective in preventing the formation of a percolation network of the redox-active O anions, leading to the topological inhibition of oxygen loss. This study offers valuable theoretical insights into the role of Li content in the control of cycling stability in LRLO cathodes.

2. Results

2.1. Thermodynamic Stability

It has been demonstrated in previous studies that the distribution of $\text{Li}@\text{Mn}_6$ structure units in the TM layer is crucial for regulating the balance between specific capacity and cycling stability of LRLO cathodes.^[19,26–28] In the layered structure, where the metal sites in the TM layer are arranged in a triangular lattice, we focus on the configurations with an evenly-distributed alignment of Li sites in this layer with sufficient separation between Li ions at different x values of $\text{Li}[\text{Li}_{1-x}\text{Mn}_x]\text{O}_2$. We find that for $x = 2/3, 3/4$, and $6/7$, a rhombic unit cell structure can be formed at ordered Li distribution, while for $x = 4/5$ and $5/6$, the Li ions can only exhibit a less evenly dispersed distribution, as shown in Figure 1. The thermodynamic stability of these ordered configurations with respect to disordered counterparts can be justified by the calculations using cluster expansion method,^[29] as shown in Figure S2 (Supporting Information).

Ligand field theory demonstrates that the d orbitals of a transition-metal ion in an octahedral complex will be split into a set of three-fold degenerate t_{2g} states and two-fold degenerate e_g states.^[30] As Mn^{3+} is at a high spin state ($t_{2g}^3 e_g^1$), the partially occupied e_g states cause the Jahn–Teller distortion of the octahedron to realize a reduction in total energy; the Mn^{4+} ($t_{2g}^3 e_g^0$), on the other hand, does not exhibit the Jahn–Teller effect. Therefore, in LiMnO_2 , as all Mn ions are $+3$ and the Jahn–Teller distortion

orientation of all Mn^{3+} remains consistent, a cooperative Jahn–Teller effect is demonstrated. In Li_2MnO_3 , as all Mn ions are $+4$, there will be no Jahn–Teller distortion. For cathode materials having a composition between these two compounds, the number of Mn^{4+} will be twice the number of Li at the TM layer, and the rest will be Mn^{3+} . The distorted Mn^{3+}O_6 octahedra share edges with the undistorted Mn^{4+}O_6 and LiO_6 octahedra, which will lead to lattice distortion of the overall structure and a corresponding decrease in thermodynamic stability. By calculating their energy convex hull, we find that these materials with lattice structural distortion are in a thermodynamic metastable state, with energy distributed around 100 meV/f.u. above the convex hull, as shown in Figure 2a.

For the case of complete delithiation, as Mn–O forms a six-coordinated octahedron, the valence state of Mn is unable to further increase and thus remains at $+4$. The corresponding O anion will be oxidized to achieve charge balance. As the Mn content in the TM layer decreases, the oxidation degree of anions will increase, and the corresponding thermodynamic stability will also be affected. Figure 2b shows that Mn_xO_2 is thermodynamically unstable with regard to the layered MnO_2 , which, however, is also unstable as compared to the β phase of MnO_2 , in agreement with the previous work.^[31] At the fully delithiated state, in addition to the O ions being oxidized individually, the oxidation can be accomplished by forming a dimer between two neighboring O ions to become $(\text{O}_2)^{2-}$. The oxygen dimers may also exist in different forms, as shown in Figure 2c. For $\text{Mn}_{2/3}\text{O}_2$, some of the generated dimers correspond to an average magnetic moment of $1 \mu_B$, and the O–O distance is 1.34 Å. For other compositions, the generated dimers tend to exhibit a magnetic moment of $0 \mu_B$ and an O–O distance of 1.45 Å, suggesting the formation of peroxide-like $(\text{O}_2)^{2-}$.^[32] The energy difference between forming oxygen dimers and forming individual O anions with a valency above -2 is always negative, as shown in Figure 2d, highlighting the participation of oxygen dimers in the redox reactions.

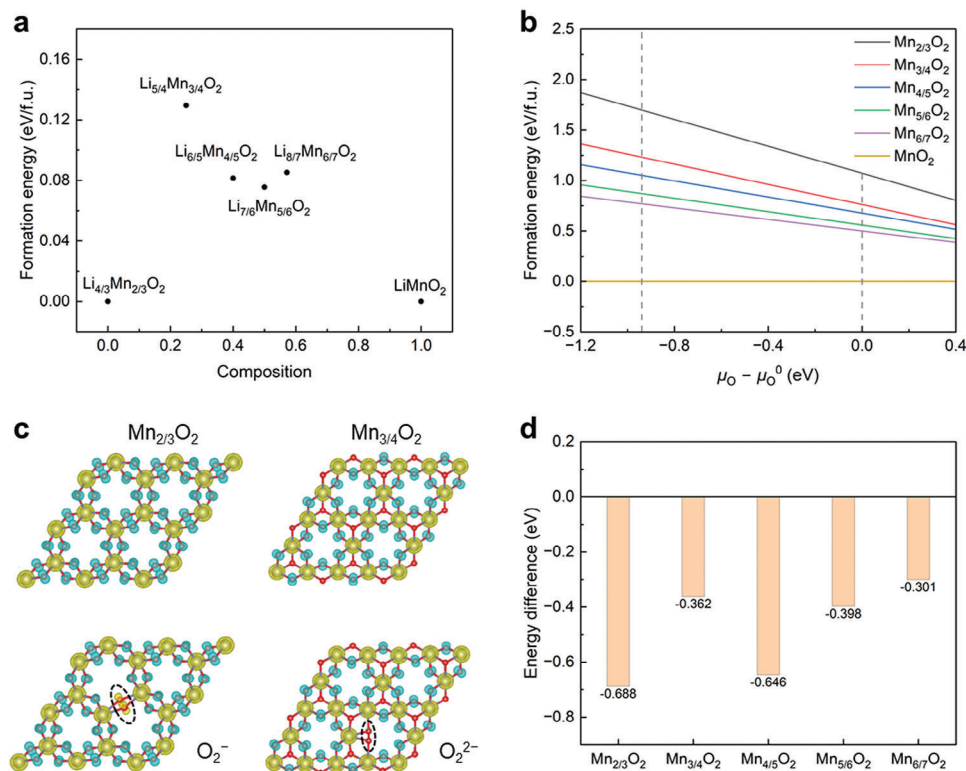


Figure 2. Thermodynamic stability of Li[Li_{1-x}Mn_x]O₂ and the oxidized O ions. a) Formation energy of Li[Li_{1-x}Mn_x]O₂ as a reference of both Li₂MnO₃ and LiMnO₂. b) Stability of Mn_xO₂ under different chemical potentials of oxygen (μ_O). c) Magnetization density distribution for the fully delithiated samples. Yellow and turquoise isosurfaces denote areas of positive and negative values ($\pm 0.05 e \text{ bohr}^{-3}$), respectively. Color code for atoms: Mn, blue; Li, green; O, red. d) The energy difference between forming oxygen dimers and forming individual O anions with a valency above -2 .

2.2. Migration of Oxygen Vacancies

When electric holes are localized at the oxidized O ions, the thermodynamic stability of these O ions can be measured by comparing the vacancy formation energy, which is closely related to the local environment of O ions. There are two local environments of O ions: one is connected to 4 Li ions and 2 Mn ions, and the other is connected to 3 Li ions and 3 Mn ions. As mentioned above, the energy level of the orphaned Li–O–Li state is higher than that of the O 2p orbits hybridized with Mn 3d orbits. These O 2p states are located at the top of the O valence band and are the first to be oxidized during the redox process. Figure S4 (Supporting Information) shows the calculated magnetic moments of O ions in the optimized structures without the formation of O dimers when all the Li ions are extracted. We can find that the magnetic moment of the O ion linked to two Mn is $\approx -0.6 \mu_B$, indicating its participation in the oxidation process, while the other type of oxygen is still maintained at a valency of -2 . The formation energy of the O vacancy is displayed in Figure 3. It is revealed that the vacancy formation energy corresponding to oxidized O is below 0.7 eV, which is lower than the corresponding value of unoxidized O (higher than 1.0 eV). In particular, in MnO₃, with vacancies accounting for one-third of the sites in the TM layer, the oxygen vacancy formation energy is less than 0 eV, meaning that this species tends to generate a large number of oxygen vacancies. Overall, when the number of Mn connected to oxygen is less than 3, this type of oxygen will be oxidized at the fully delithiated

state, and the corresponding vacancy formation energy will also be reduced. Therefore, this type of oxygen ions can be regarded as redox-active, while those connected to three Mn cations are termed redox-inactive.

The efficiency of O migration in the bulk of LRLO cathodes is crucial because it dictates the ability of the oxygen dimer to approach the surface region. The capability of O vacancies

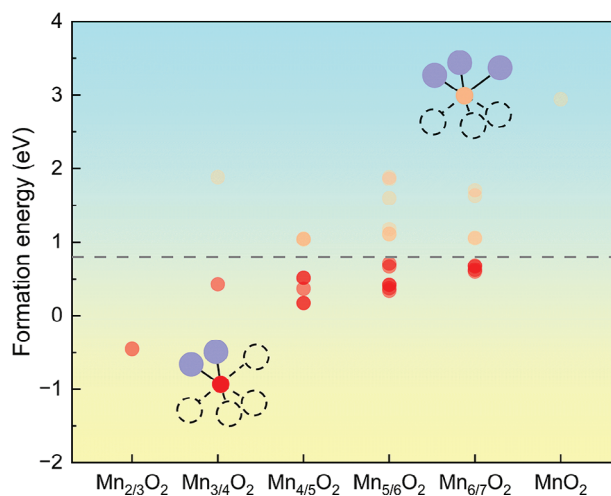


Figure 3. Formation energy of oxygen vacancy in different local environments at the fully delithiated state of Li[Li_{1-x}Mn_x]O₂.

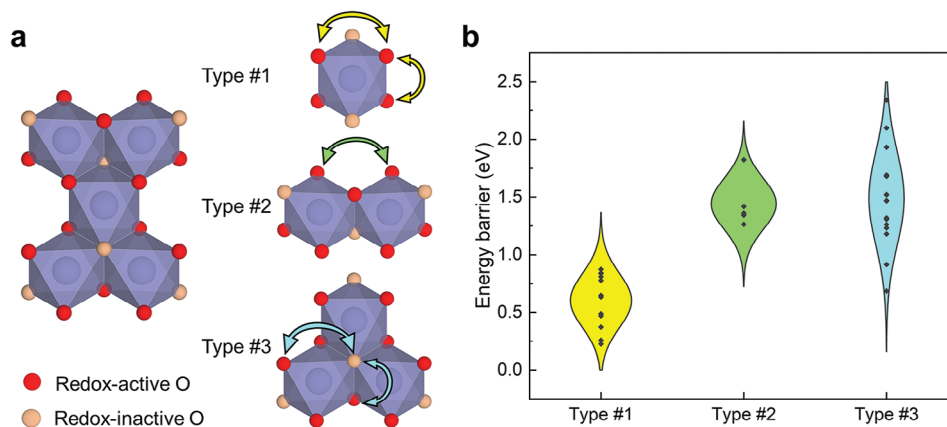


Figure 4. Migration of O vacancies at the fully delithiated state of $\text{Li}[\text{Li}_{1-x}\text{Mn}_x]\text{O}_2$. a) Schematics of three kinds of migration paths. b) Distribution of activation energy barriers for different migration paths.

to migrate in the anion sublattice influences whether these O ions remain localized within the bulk structure or can be easily released.^[33–36] This migration ability is a critical aspect that determines the dynamic behavior of O ions within the material. In the following, we use the climbing-image nudged elastic band (CI-NEB) method to evaluate the activation barrier for the migration of O vacancies.

Due to the intimate connection between the redox activity and the thermodynamic stability of O ions in their local environment, we categorize the potential migration paths of O ions in the bulk phase as follows. In LRLO cathodes, the anion sublattice is shaped by the face-centered-cubic (FCC) arrangement of O ions. Cations, including transition metals and alkali metals, occupy the central positions of the octahedra, and the edges of these octahedra determine the migration path of O ions. When the cathode material is at the fully delithiated state, the following three types of migration paths will emerge, as displayed in **Figure 4a**: 1) The migration path is located between two redox-active O ion sites, and both sites are at the same Mn–O octahedron. There are two paths in this type: one is along the edges of the Mn–O octahedron in different anion layers, and the other is within the same anion layer. 2) The migration path is located between two redox-active O ion sites, and these sites are from different Mn–O octahedra. 3) The migration path is located between one redox-active O ion site and one redox-inactive O ion site, and both sites are at the same Mn–O octahedron.

The distribution of the activation energy barriers is depicted in **Figure 4b**. We note that the energy barrier for O ions to overcome in the first type of migration path is generally lower than the other two paths. We also explore the possibility of redox-active O ions migrating between the adjacent TM–O slabs. The results, as shown in **Figure S6** (Supporting Information), indicate that this kind of migration path becomes unfavorable when the Li ions are completely extracted. The above results suggest that, when considering the migration process of O ions in the bulk phase, it is necessary to emphasize on the network formed by the redox-active O ions in the Mn–O octahedra, while other migration paths can be ignored in the following calculations.

2.3. Migration of Transition Metal Ions

The phenomena of voltage hysteresis and capacity fading during the cycling process of LRLO cathodes have been extensively investigated both experimentally and theoretically.^[26,37–39] It is believed that these processes are closely associated with the irreversible migration of TM ions coupled with oxygen release. When the structure units of the $\text{Li}@\text{Mn}_6$ are adjacent, the migration of Mn to the nearest-neighbor Li site in the TM layer can lead to a configuration where multiple LiO_6 octahedra exhibit an aggregated pattern, resulting in the emergence of dangling O ions (the O ion is connected to only one Mn ion). In the charged state, these oxygen ions tend to form dimers to facilitate the oxidation process.^[40,41] Here, we try to determine whether these dangling oxygen ions form dimers during TM intralayer migration and assess the impact of this phenomenon on the thermodynamic energy change of the system, as well as the corresponding energy barriers required for TM intralayer migration.

The calculated activation barriers for TM migration are provided in **Figure 5a**, taking multiple paths and local environments into consideration. For the structure of Li_2MnO_3 , the entire TM layer is densely packed with the structure units of $\text{Li}@\text{Mn}_6$. When a Mn ion migrates to the neighboring vacant site at the delithiated state, it will introduce four dangling O ions. As all O ions in MnO_3 are oxidized, the layer spacing between two TM layers also decreases significantly. After structural optimization, spontaneous formation of numerous oxygen dimers between TM layers occurs, leading to a substantial decrease in the energy of the final state after TM migration. As the x in $\text{Li}[\text{Li}_{1-x}\text{Mn}_x]\text{O}_2$ increases and the concentration of $\text{Li}@\text{Mn}_6$ structure units becomes lower, the possibility of TM migration leading to the aggregation of vacant sites in the TM layer continuously decreases. There are two types of arrangement of hexagonal rings where a single migration event can form aggregated vacant sites in the TM layer, as shown in **Figure 5b**. One is characterized by a common edge, which can be found in $\text{Mn}_{2/3}\text{O}_2$ and $\text{Mn}_{4/5}\text{O}_2$. The other corresponds to connection via a common vertex, found in $\text{Mn}_{3/4}\text{O}_2$ and $\text{Mn}_{5/6}\text{O}_2$. The same trend is illustrated for all compositions, and at $x = 6/7$, the aggregation of vacancy sites in the

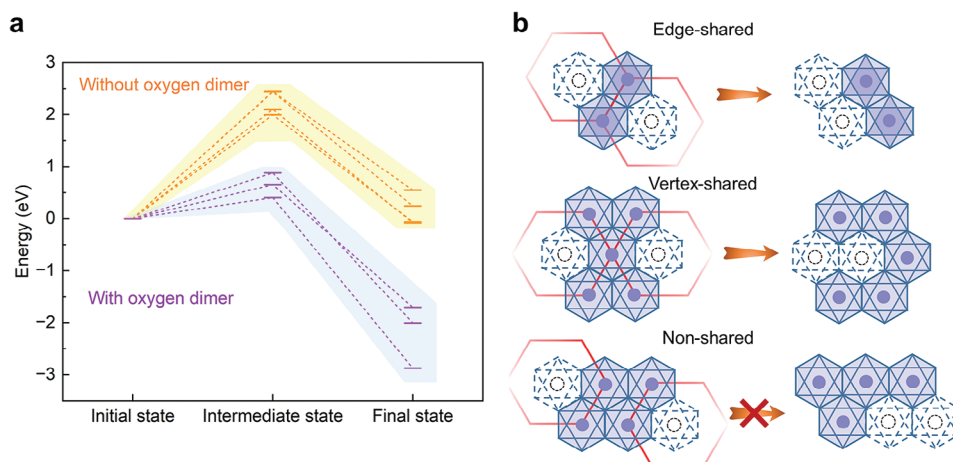


Figure 5. Migration of TM ions at the fully delithiated state of $\text{Li}[\text{Li}_{1-x}\text{Mn}_x]\text{O}_2$. a) Activation barriers for the migration of TM ions in different paths and configurations. b) Two types of arrangement of $\text{Li}@\text{Mn}_6$ structure units, where a single migration event can form aggregated vacant sites in the TM layer, and one type of arrangement that cannot lead to this aggregation.

TM layer cannot be achieved through a single migration step because each pair of neighboring $\text{Li}@\text{Mn}_6$ is not shared by edge or vertex.^[42–44] After the aggregation of the vacant sites, two nearby dangling O ions can form an oxygen dimer in the TM-O slabs, and its formation will significantly reduce the thermodynamic energy of the structure. By calculating the activation energy barrier of migration according to whether there is an oxygen dimer in the final state, it is found that the presence of oxygen dimers effectively reduces the difficulty of TM migration. This result can be explained as the formation of oxygen dimer is synchronized to the migration of Mn; therefore, the energy released in the former process can compensate for the energy consumption during the latter process. This energy compensation is manifested by the reduction in the activation barrier, as shown in Figures S7–S9 (Supporting Information). Figure 5a reveals that the TM migration accompanied by the generation of oxygen dimer can reduce the TM migration energy barrier from above 2 eV to below 0.9 eV.

2.4. Percolation Network of Redox-Active Oxygen Ions

For a regular lattice, the percolation model considers a network with randomly occupied sites (vertices) or bonds (edges) with statistically independent probability.^[45–48] There is a critical threshold concentration, at which large clusters and long-distance connectivity begin to emerge. In other words, the connection probability p_c , indicating the likelihood of a continuous path from one boundary to another along occupied sites or bonds within a single cluster, is used to calculate the percolation threshold. Depending on the method of how to generate the random network, a distinction can be made between the site percolation threshold and bond percolation threshold. Based on the problem we focused on in this work, during oxygen release, the oxidized O ions require the existence of pathways through which they can migrate to the surface region. Therefore, we define p_c as the proportion of the connected clusters formed between the occupied sites that can connect to the surface region. We show a schematic diagram (Figure 6a) of whether the connected clusters formed be-

tween occupied sites under different site concentrations (α) can be linked to the system boundary. It can be seen that in the 2D honeycomb network, as the site concentration changes from 0.5 to 0.9, the degree of percolation of the network composed of occupied sites continues to increase, and after exceeding the percolation threshold, the entire network becomes fully connected to the boundary. For the percolation problem in a lattice with infinite size, the exact value of the percolation threshold can be derived for specific 2D lattices (e.g., the site percolation threshold of a 2D triangular lattice is 0.5). In the case of complex lattices, the approximate percolation threshold values can be obtained via Monte Carlo simulations.^[49]

During the numerical simulation process, we usually use a finite size of the lattice to extrapolate the result of the infinite size. The function between the connection probability p_c of the percolation network and the proportion of site occupations is sigmoidal, as shown in Figure 6b. As the size of the 2D honeycomb lattice continues to increase from 96×96 to 480×480 , the corresponding connectivity probability function will gradually approach the step function at the percolation threshold. We can obtain an approximated threshold value of 0.7, which is consistent with previous studies.^[50,51] We also calculate the fraction of the occupied sites that are part of the percolation network. In the finite-size lattice employed for the numerical simulation, each occupied site either belongs to the percolation cluster which can connect to the lattice boundary or to the finite isolated cluster which is surrounded by other unoccupied sites. P is the ratio of the number of sites in the percolation cluster to the total number of occupied sites. Once the site concentration is above the percolation threshold, the number of sites in the percolation cluster will approach the number of occupied sites and the P - α curves become $P = \alpha$ (Figure 6c).

In order to apply the percolation theory to the problem of O ions migrating through the anion sublattice in LRLO to be released at the material surface, we need to consider the potential migration of O ions in different local environments. Based on the first-principles calculations of O ion migration barriers discussed above, the potential migration paths of O ions are those between

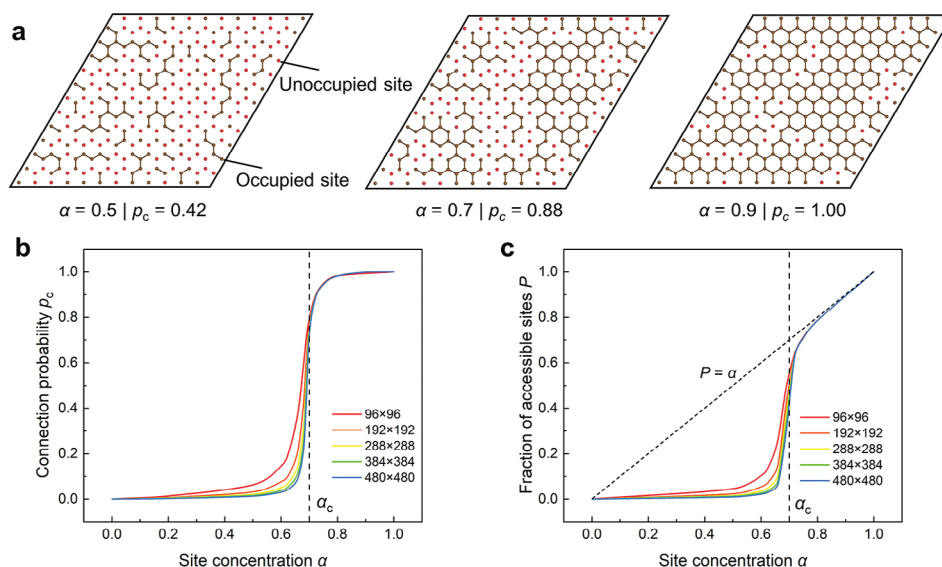


Figure 6. The percolation problem of occupied sites in a 2D honeycomb network. a) Schematics of non-percolating and percolating cases at different site concentrations α . b) Connection probability p_c of the percolation network as a function of the site concentration α . c) Fraction of accessible sites P as a function of the site concentration α .

two redox-active O sites, while satisfying the condition that both sites are connected by an edge of the same MnO_6 octahedron. Moreover, the aggregation of vacant sites in the TM layer will cause the O ions to form dimers upon delithiation. To simplify the complex situation of the existence of oxygen dimers when studying the O migration network, we regard the nearest neighbor paths between O ions around the aggregated vacant sites as connectable. Therefore, in the percolation network composed of O ions, we assume that the proportion of redox-active O ions represents the occupied site ratio. At the same time, whether these O ions are redox-active or not is determined by the local coordination environment. Two redox-active O sites can only be connected if there is an active diffusion channel between these sites. In addition, as O ions are difficult to migrate between different TM layers at a fully delithiated state, we only focus on the percolation of O ions within the same TM-O slab. This network can be simplified into a 2D honeycomb-like lattice, with two possible connection modes: nearest-neighbor and next-nearest-neighbor connections, corresponding to paths between different O layers and paths within the same layer, respectively. As the redox activity of oxygen is related to its local environment, we can control the proportion of redox-active O ions by regulating the content x of Mn in the TM layer. We focus on the following two scenarios in the percolation problem: first, considering a completely random arrangement of TM ions; second, based on the initial state of ordered TM arrangements, simulating the percolation network with different x by exchanging the positions of TM and Li sites within the layers, mimicking the migration of TM ions within the TM layer in long-term cycling. We perform Monte Carlo simulations to determine the percolation threshold and the accessible O content as a function of x .

In the first scenario, starting from a configuration with the TM layer entirely occupied by Mn ions, some of the Mn ions are then randomly replaced with Li ions, in accordance with the composition of this LRLO. Based on the generated structure, the lo-

cal coordination environment of O ions is assessed to determine whether it is redox-active: the anion is considered redox-active if it is connected to less than three Mn ions, as defined above; otherwise, it is redox-inactive. Then, pathways of O migration between two (next-)nearest-neighbor redox-active O sites are formed, and it is ensured that these two sites are connected to the same Mn ion to create a continuous pathway.

Figure 7a,b shows the schematic diagrams of the network formed by redox-active O ions in a small-size simulation cell when the proportions of Mn in the TM layer are 3/4 and 5/6 respectively. The statistical result in Figure 7c shows that when x is 2/3 or 3/4, the proportion of redox-active O ions significantly exceeds the percolation threshold, meaning that it is very likely for the redox-active oxygen ions to migrate to the surface and be released through the percolation network. When x is 5/6 or 6/7, the ratio of redox-active O ions is lower than the percolation threshold, and a large number of O ions will be encaged inside the material and difficult to release. For $x = 4/5$, which is slightly less than the percolation threshold, there is a great possibility of oxygen ions being released when the size of the simulation cell is not large enough. Besides, we note that the p_c of O ions and the proportion of redox-active O species still have a sigmoidal form that is similar to Figure 6b. Despite that the Mn ions are randomly arranged, there is a stable correspondence between the proportion of redox-active O ions and the proportion of Mn in the TM layer, regardless of the size of the simulation cell.

In the second scenario, the initial structure is constructed based on the ordered arrangement of Mn ions. To simplify the migration paths of Mn ions, only the impact of intralayer migration is considered. As the migration of Mn is accompanied by the formation of O dimers, we simplify the migration process in MC simulation to the determination of whether the migration contributes to the increase in aggregated vacant sites in the TM layer at the delithiated state. As mentioned above, this aggregation will increase the number of dangling O ions and

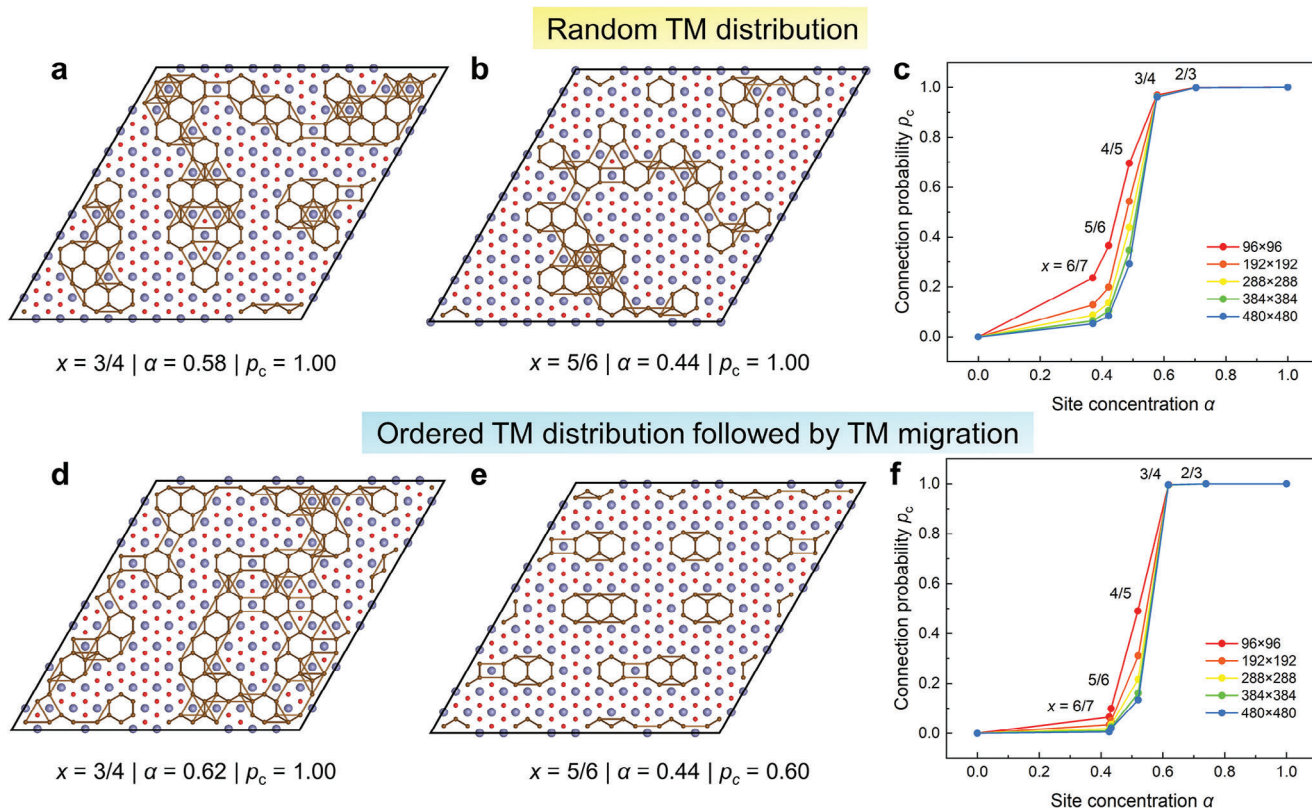


Figure 7. The percolation problem of redox-active O ions in $\text{Li}[\text{Li}_{1-x}\text{Mn}_x]\text{O}_2$ with two kinds of TM distribution in the lattice. a) $x = 3/4$, b) $x = 5/6$ configurations, and c) the connection probability p_c of the percolation network in the scenario of random TM distribution. d) $x = 3/4$, e) $x = 5/6$ configurations, and f) the connection probability p_c of the percolation network in the scenario of an initially ordered structure where TM ions can migrate to adjacent sites afterward.

facilitate the formation of dimers. Therefore, we randomly select one vacant site, and exchange this site with a nearby Mn site if the Mn migration can lead to the aggregation of vacant sites. Otherwise, the exchange will not be conducted. The number of possible steps for such an operation scales with the number of vacant sites in the TM layer, which is reminiscent of the TM migration in LRLCO cathodes under long-term cycling. Similar to the first scenario (random TM distribution), the corresponding percolation network of redox-active O ions can be obtained based on the arrangement of Mn. The one-to-one correspondence between the proportion of redox-active O ions and the Mn content is still satisfied. In the ordered structure, as the number of Mn ions connected with an O ion is either 2 or 3, it has the largest proportion of redox-active O, excluding the dangling species. Accordingly, the increase in the aggregated vacant sites in the TM layer obtained by exchanging the positions of Mn ions will lead to the reduction of the proportion of redox-active O ions. Therefore, the number of site-exchanging steps will significantly affect the distribution of redox-active O ions. Figure S10 (Supporting Information) shows the trend in the proportion of redox-active O ions in the system and the corresponding connection probability p_c when the number of exchanges is zero, one-tenth of the number of vacant sites, and the exact number of vacant sites, respectively.

As the number of site-exchanging steps increases, the points corresponding to different Mn contents continue to move toward lower values on the p_c - α curve. In other words, the Mn content

required to inhibit system percolation will also decrease as the number of site-exchanging steps increases. The corresponding Mn content near the percolation threshold decreases upon the continuous site exchange and will finally reach 5/6 with the number of site-exchanging steps equal to the number of vacant sites in the TM layer. The corresponding statistical results are displayed in Figure 7f. Similar to the conclusion drawn in the first scenario, the Mn ratios in the TM layer above the percolation threshold include 2/3 and 3/4 (Figure 7d), the ratios below the threshold are 5/6 and 6/7 (Figure 7e), and the ratio near the threshold is 4/5. More importantly, as there is no shared edge/vertex between any two Li@Mn_6 structure units in the $\text{Mn}_{6/7}\text{O}_2$ configuration, it is difficult for Mn to migrate within the layer, resulting in the redox-active O ions being uniformly confined in the interior of the bulk phase. The p_c is slightly larger than zero because O ions at the surface of the finite-size lattice are included in the statistical calculations. Interestingly, at $x = 5/6$, all the redox-active O ions can migrate to the surface at the initial state before the site-exchanging steps, as shown in Figure S11 (Supporting Information), for which the connection probability p_c is 1.0. However, after Mn migration, the integrity of the redox-active O ion migration network is disrupted, leading to a continuous decrease in the connection probability. Notably, when the material size is sufficiently large and the Mn migration has fully taken place, the $\text{Li}_{7/6}\text{Mn}_{5/6}\text{O}_2$ cathode can topologically inhibit the irreversible release of O ions in the lattice.

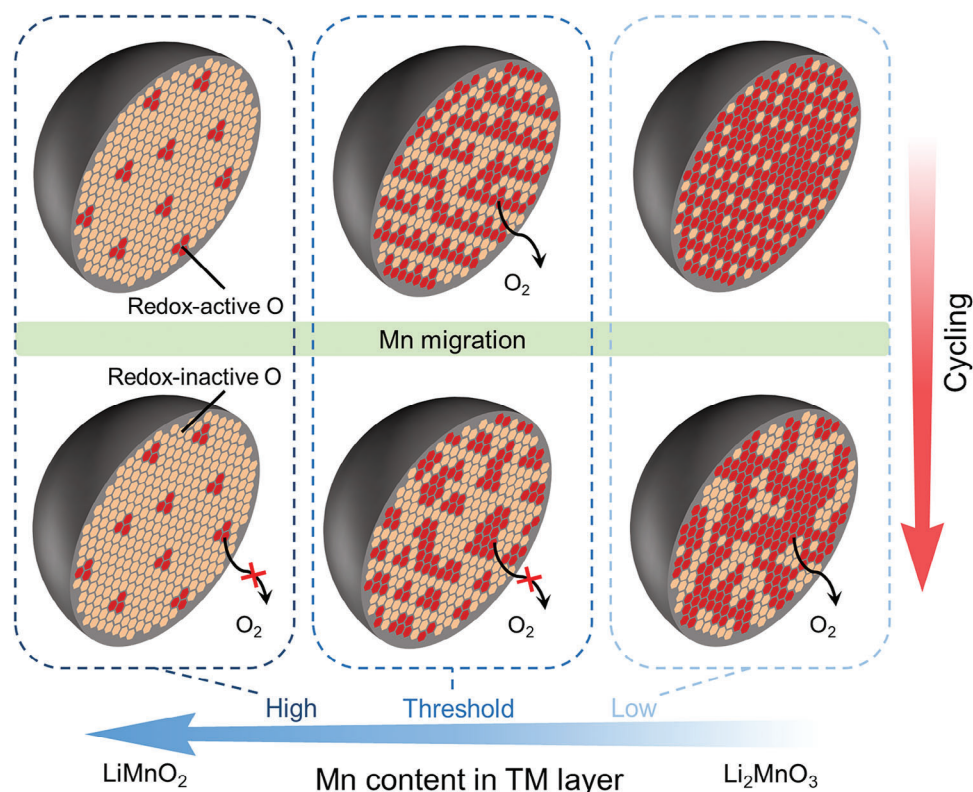


Figure 8. Schematic diagram of the distribution of redox-active oxygen ions in $\text{Li}[\text{Li}_{1-x}\text{Mn}_x]\text{O}_2$. As the Mn content x increases from $2/3$ to 1 , the connection probability p_c of the percolation network composed of redox-active O ions gradually decreases (from $p_c = 1$ to 0). Mn migration in the TM layer leads to the redistribution of the redox-active O ions, thus affecting their connectivity, especially when x is close to the threshold value.

3. Discussion and Conclusion

During the cycling process of LRLO cathodes, oxygen loss is closely related to the kinetics of O ion migration in the lattice, mainly in the form of the migration of O vacancies from the surface to the interior region of the particle. Hence, the most pivotal strategy for mitigating oxygen loss lies in obstructing the migration pathway of O ions to the surface. Up to now, surface modification methods have been extensively employed to hinder the migration of O ions in the surface region, which was shown effective in suppressing oxygen loss.^[52–54] However, such methods can induce pernicious internal strain due to lattice incompatibility, and consequently, the inhomogeneous expansion and contraction at the interface during cycling may trigger delamination and disintegration of the cathode material. In this work, utilizing first-principles calculations in combination with percolation theory and Monte Carlo simulations, we unveil the relationship between the local environments and the migration pathways of O ions in $\text{Li}[\text{Li}_{1-x}\text{Mn}_x]\text{O}_2$ cathode materials. Our results indicate that the redox-active O ions can be engaged in the bulk phase of $\text{Li}[\text{Li}_{1-x}\text{Mn}_x]\text{O}_2$ with x exceeding $5/6$, due to the failure of forming a percolation network for O ions migrating to the surface. This ability of topologically inhibiting oxygen loss in the bulk phase can be regarded as an intrinsic property of the cathode material itself, which can avoid the lattice strain problem in surface modification approaches. From the insights of our results, the following strategies for mitigating oxygen loss are provided: i) the

ratio of TM ions in TM layer should be no less than $5/6$, while the Li ions in TM layer should be uniformly distributed (i.e., in a delocalized distribution pattern); ii) Mn migration and oxygen release can be decoupled in the activation process of the first few cycles to promote the former and minimize the latter; and iii) special superstructures (i.e., specific kinds of ordered Li/Mn pattern in the TM layer) may be designed to surpass the theoretical capacity of $\text{Li}_{7/6}\text{Mn}_{5/6}\text{O}_2$ while preventing the percolation of redox-active O ions.

We would like to note that some previous studies have already discovered the essential role of the distribution of $\text{Li}@\text{Mn}_6$ structure units on the cycling stability of LRLO cathodes.^[19,27,28,44] A delocalized distribution pattern was demonstrated to be beneficial in preventing the formation of large voids in the lattice, which are related to the aggregation of vacant sites in the TM layer, as shown in Figure 5b. In contrast, a localized distribution pattern of $\text{Li}@\text{Mn}_6$ would lead to continuous growth of the large voids, which will finally reach the surface and trigger oxygen release. To enable the formation of a delocalized distribution pattern, the content of Li ions in the TM layer should not be too high. Based on this consideration, a recent study has reported an LRLO cathode with $x = 6/7$, which exhibits an ordered cation arrangement in the TM layer and can successfully restrain oxygen release.^[44] Yet, it remains elusive whether there is a threshold of composition, under which the inhibition of oxygen release is guaranteed upon delocalized distribution of $\text{Li}@\text{Mn}_6$. In this work, we have provided an answer to the above question. We show that

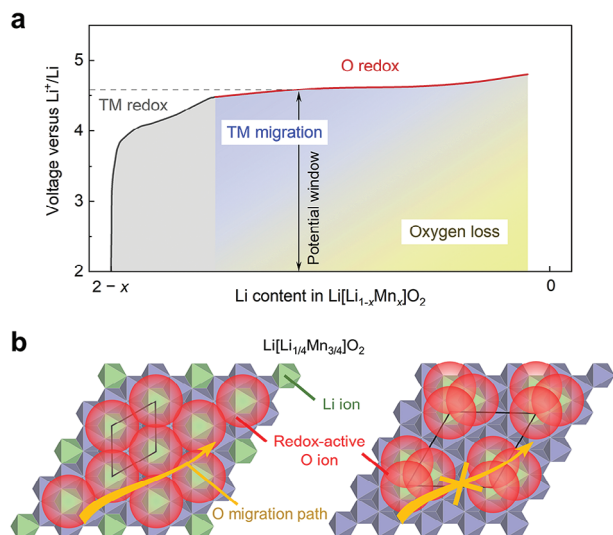


Figure 9. Strategies for inhibiting oxygen loss in LRLO cathodes. a) Schematic voltage profile of an LRLO cathode. The activation process for the first few cycles should be limited in a potential window before oxygen release, so that Mn migration can take place without the influence of oxygen loss, which would be beneficial for preventing the formation of the redox-active O percolation network. b) Two kinds of Li/Mn distribution patterns in the TM layer of $\text{Li}_{5/4}\text{Mn}_{3/4}\text{O}_2$. The left panel shows the fully delocalized distribution of Li@Mn_6 structure units that results in the percolation of redox-active O ions. The right panel shows a superstructure with three aggregated Li sites distributed uniformly in the lattice, which corresponds to a well-separated distribution pattern of the redox-active O ions.

this threshold corresponds to $x = 5/6$, and Mn content above this value could create intrinsic barriers to limit the growth of aggregated vacant sites in the TM layer, whereby the redox-active O ions are disconnected and the O migration paths to the surface are obstructed (Figure 8). On the other hand, cathodes with Mn content below $5/6$ in TM layer can hardly prevent the formation of a percolation network of the redox-active O ions and will inevitably suffer from oxygen loss during cycling if surface coating is not employed. We believe that this threshold value could provide a theoretical guideline for the rational compositional design of LRLO cathodes.

The reason that Mn migration and oxygen release may be decoupled is clear from our calculation results of the activation energy barriers displayed in Figures 4 and 5. We note that the energy barriers of O migration between two redox-active O sites ($\approx 0.2\text{--}0.8\text{ eV}$) are in a similar range to that of Mn migration with the formation of oxygen dimers. It means that the difference in diffusivity between Mn and O ions is not significant. However, oxygen loss requires the long-range migration of O ions and only the redox-active ones can participate in this process, while Mn migration corresponds to the short-range hopping event between two neighboring octahedral sites. The only prerequisite for Mn migration is the simultaneous formation of oxygen dimers, which is found to be highly exothermic from our DFT calculations (Figure 2d; Figures S8 and S9, Supporting Information). Therefore, in the voltage plateau of O redox, intralayer migration of Mn would likely proceed before oxygen loss, especially in the interior region of the cathode material (Figure 9a). According to

our MC simulations at $x = 5/6$ (Figure 7; Figure S11, Supporting Information), the migration of Mn ions can lead to the aggregation of vacant sites in a relatively delocalized distribution pattern, which disrupts the redox-active O percolation network that tends to emerge before delithiation. Therefore, we propose a strategy that the cathode material should undergo activation for the first few cycles in a potential window before oxygen release, whereby Mn migration can take place without any structural changes conferred by oxygen loss. Nevertheless, as the number of oxygen dimers formed in this potential window will be relatively lower than that at the fully delithiated state, the occurrence of Mn migration would be quite limited. Additional tactics should therefore be incorporated to further promote Mn mobility in this activation stage.

Our results also suggest that it is feasible to tune the connection of redox-active O ions by facilitating the ordering of metal ions in the TM layer. As mentioned above, a uniform distribution of Li ions in the TM layer in $\text{Li}[\text{Li}_{1-x}\text{Mn}_x]\text{O}_2$ will benefit the separation of redox-active O ions, thus hindering the formation of a percolation network. This inspires us to speculate that there can be some kinds of ordered Li/Mn pattern in the TM layer to achieve a non-percolating configuration of redox-active O ions with x lower than $5/6$. Mn migration should be prevented in this configuration; otherwise, the uniform distribution pattern cannot be preserved during cycling. Figure 9b shows an example of such configuration at a composition of $\text{Li}_{5/4}\text{Mn}_{3/4}\text{O}_2$. Notably, if the Li@Mn_6 structure units are fully delocalized in the TM layer, a percolation network of redox-active O ions will emerge and be preserved upon Mn migration. However, for a superstructure with three aggregated Li sites distributed uniformly, the percolation network no longer exists, while the migration of Mn is prohibited because it cannot trigger the formation of an additional oxygen dimer (a dimer has already been formed in the middle of these aggregated Li sites upon delithiation). Therefore, designing an LRLO cathode material with a special Li/TM superstructure in the TM layer may offer opportunities to achieve topological inhibition of oxygen loss with x across the threshold value.

4. Experimental Section

First-Principles Calculation: All the calculations were performed using the plane-wave based density functional theory method, as implemented in the Vienna ab initio simulation package (VASP).^[55–57] The Perdew–Burke–Ernzerhof (PBE) form of generalized gradient approximation (GGA) based on projector-augmented wave (PAW) method was selected to describe the electronic exchange–correlation potential.^[58–60] A cutoff energy was set as 520 eV and the electronic energy convergence criterion was set as 10^{-5} eV. In all the calculations, the Brillouin zone was sampled by Monkhorst–Pack k-point grid with a density of at least 25 points per \AA^{-3} . In order to correctly characterize the localization of transition-metal *d*-electrons, the GGA + *U* method was used to account for the strong correlation interactions.^[60–62] The value for the Hubbard *U* parameter of Mn was 4.2 eV.^[63] Geometries were optimized until the forces on the atoms were less than 0.02 eV \AA^{-1} . The spin polarization was taken into consideration. All calculations were performed based on an initial configuration of the ferromagnetic ordering of Mn atoms. DFT-D3 semi-empirical van der Waals correction was applied to deal with the dispersion force during structural relaxation.^[64] The migration barriers of ions were calculated using the CI-NEB method.^[65]

To examine the thermodynamic stability of oxygen, the oxygen vacancy formation energy was calculated, which is defined as $E(V_O) = E(\text{Mn}_x\text{O}_{2-\delta}) + \delta/2E(\text{O}_2) - E(\text{Mn}_x\text{O}_2)$, where $E(\text{Mn}_x\text{O}_{2-\delta})$ and $E(\text{Mn}_x\text{O}_2)$ are the total energies of the transition metal oxides with oxygen vacancy and without oxygen vacancy, respectively. $E(\text{O}_2)$ is the total energy of an oxygen molecule. To correct for self-interaction errors within DFT, an energy correction of -1.36 eV for the O_2 molecule was used in the calculations.^[63,66]

Monte Carlo Simulation: Monte Carlo simulations were used to investigate the oxygen percolation probability coupled with the fraction of redox-active O ions and Mn occupation in the TM layer. In MC simulations, a network of redox-active O sites was considered percolating when it linked to the periodic boundaries of the simulation cell in one or more directions. This network could be simplified into a 2D honeycomb network and its size was set from 96×96 to 480×480 to obtain statistical results, which corresponded to 18 432–460 800 anions in the lattice. In order to evaluate the oxygen percolation probability p_c under a specific Mn content x , two MC simulations were performed according to different assumptions (random TM distribution or ordered TM distribution followed by TM migration).^[49]

For the case of random TM distribution, an MC sweep was performed as follows: i) a 2D triangle network was initialized with a configuration full of Mn atoms, ii) Mn atoms were randomly changed to Li (vacancy) until the specified ratio was reached, iii) the 2D honeycomb network of oxygen was constructed by the triangle network, and the occupied oxygen concentration α and the connection probability p_c were calculated.

For the case of ordered TM distribution followed by TM migration, an MC sweep was performed as follows: i) a 2D triangle network was initialized with an ordered arrangement of Mn atoms in a specific proportion, ii) the vacant sites were exchanged with an adjacent Mn site by a certain number, iii) the 2D honeycomb network of oxygen was constructed by the triangle network, and the occupied oxygen concentration α and the connection probability p_c were calculated.

The values of p_c and α at different x were averaged over 1000 MC sweeps to guarantee well-converged estimates.

Supporting Information

Supporting Information is available from the Wiley Online Library or from the author.

Acknowledgements

The authors acknowledge financial support from the Soft Science Research Project of Guangdong Province (No. 2017B030301013), the National Natural Science Foundation of China (22109003), the Basic and Applied Basic Research Foundation of Guangdong Province (2021B1515130002 and 2023A1515011391), and the Major Science and Technology Infrastructure Project of Material Genome Big-science Facilities Platform supported by Municipal Development and Reform Commission of Shenzhen.

Conflict of Interest

The authors declare no conflict of interest.

Data Availability Statement

The data that support the findings of this study are available from the corresponding author upon reasonable request

Keywords

density function theory, Li-rich cathodes, Monte Carlo simulations, oxygen loss, percolation theory

Received: March 4, 2024
Revised: April 15, 2024
Published online: April 23, 2024

- [1] M. Li, J. Lu, Z. Chen, K. Amine, *Adv. Mater.* **2018**, *30*, 1800561.
- [2] J. Liu, J. Wang, Y. Ni, K. Zhang, F. Cheng, J. Chen, *Mater. Today* **2021**, *43*, 132.
- [3] G.-L. Zhu, C.-Z. Zhao, J.-Q. Huang, C. He, J. Zhang, S. Chen, L. Xu, H. Yuan, Q. Zhang, *Small* **2019**, *15*, 1805389.
- [4] A. Van der Ven, Z. Deng, S. Banerjee, S. P. Ong, *Chem. Rev.* **2020**, *120*, 6977.
- [5] J. Lee, D. A. Kitchaev, D.-H. Kwon, C.-W. Lee, J. K. Papp, Y.-S. Liu, Z. Lun, R. J. Clément, T. Shi, B. D. McCloskey, J. Guo, M. Balasubramanian, G. Ceder, *Nature* **2018**, *556*, 185.
- [6] J.-L. Shi, D.-D. Xiao, M. Ge, X. Yu, Y. Chu, X. Huang, X.-D. Zhang, Y.-X. Yin, X.-Q. Yang, Y.-G. Guo, L. Gu, L.-J. Wan, *Adv. Mater.* **2018**, *30*, 1705575.
- [7] M. Li, T. Liu, X. Bi, Z. Chen, K. Amine, C. Zhong, J. Lu, *Chem. Soc. Rev.* **2020**, *49*, 1688.
- [8] S.-L. Cui, M.-Y. Gao, G.-R. Li, X.-P. Gao, *Adv. Energy Mater.* **2022**, *12*, 2003885.
- [9] W. Zuo, M. Luo, X. Liu, J. Wu, H. Liu, J. Li, M. Winter, R. Fu, W. Yang, Y. Yang, *Energy Environ. Sci.* **2020**, *13*, 4450.
- [10] D.-H. Seo, J. Lee, A. Urban, R. Malik, S. Kang, G. Ceder, *Nat. Chem.* **2016**, *8*, 692.
- [11] B. Li, D. Xia, *Adv. Mater.* **2017**, *29*, 1701054.
- [12] M. Okubo, A. Yamada, *ACS Appl. Mater. Interfaces* **2017**, *9*, 36463.
- [13] G. Assat, J.-M. Tarascon, *Nat. Energy* **2018**, *3*, 373.
- [14] M. Ben Yahia, J. Vergnet, M. Saubanière, M.-L. Doublet, *Nat. Mater.* **2019**, *18*, 496.
- [15] J.-H. Song, G. Yoon, B. Kim, D. Eum, H. Park, D.-H. Kim, K. Kang, *Adv. Energy Mater.* **2020**, *10*, 2001207.
- [16] J. Vinckeviciute, D. A. Kitchaev, A. Van der Ven, *Chem. Mater.* **2021**, *33*, 1625.
- [17] W. E. Gent, K. Lim, Y. Liang, Q. Li, T. Barnes, S.-J. Ahn, K. H. Stone, M. McIntire, J. Hong, J. H. Song, Y. Li, A. Mehta, S. Ermon, T. Tylicszczak, D. Kilcoyne, D. Vine, J.-H. Park, S.-K. Doo, M. F. Toney, W. Yang, D. Prendergast, W. C. Chueh, *Nat. Commun.* **2017**, *8*, 2091.
- [18] D. Eum, B. Kim, S. J. Kim, H. Park, J. Wu, S.-P. Cho, G. Yoon, M. H. Lee, S.-K. Jung, W. Yang, W. M. Seong, K. Ku, O. Tamwattana, S. K. Park, I. Hwang, K. Kang, *Nat. Mater.* **2020**, *19*, 419.
- [19] W. Huang, C. Lin, J. Qiu, S. Li, Z. Chen, H. Chen, W. Zhao, G. Ren, X. Li, M. Zhang, F. Pan, *Chem* **2022**, *8*, 2163.
- [20] K. Zhang, B. Li, Y. Zuo, J. Song, H. Shang, F. Ning, D. Xia, *Electrochem. Energy Rev.* **2019**, *2*, 606.
- [21] P. M. Csernica, S. S. Kalirai, W. E. Gent, K. Lim, Y.-S. Yu, Y. Liu, S.-J. Ahn, E. Kaeli, X. Xu, K. H. Stone, A. F. Marshall, R. Sinclair, D. A. Shapiro, M. F. Toney, W. C. Chueh, *Nat. Energy* **2021**, *6*, 642.
- [22] G. Sun, F.-D. Yu, C. Zhao, R. Yu, S. Farnum, G. Shao, X. Sun, Z.-B. Wang, *Adv. Funct. Mater.* **2021**, *31*, 2002643.
- [23] Z. Li, Y. Li, M. Zhang, Z.-W. Yin, L. Yin, S. Xu, C. Zuo, R. Qi, H. Xue, J. Hu, B. Cao, M. Chu, W. Zhao, Y. Ren, L. Xie, G. Ren, F. Pan, *Adv. Energy Mater.* **2021**, *11*, 2101962.
- [24] Y. Li, S. Xu, W. Zhao, Z. Chen, Z. Chen, S. Li, J. Hu, B. Cao, J. Li, S. Zheng, Z. Chen, T. Zhang, M. Zhang, F. Pan, *Energy Storage Mater.* **2022**, *45*, 422.
- [25] Z. Zhu, D. Yu, Y. Yang, C. Su, Y. Huang, Y. Dong, I. Waluyo, B. Wang, A. Hunt, X. Yao, J. Lee, W. Xue, J. Li, *Nat. Energy* **2019**, *4*, 1049.
- [26] R. A. House, U. Maitra, M. A. Pérez-Osorio, J. G. Lozano, L. Jin, J. W. Somerville, L. C. Duda, A. Nag, A. Walters, K.-J. Zhou, M. R. Roberts, P. G. Bruce, *Nature* **2020**, *577*, 502.

- [27] J. Hwang, S. Myeong, W. Jin, H. Jang, G. Nam, M. Yoon, S. H. Kim, S. H. Joo, S. K. Kwak, M. G. Kim, J. Cho, *Adv. Mater.* **2020**, *32*, 2001944.
- [28] J. Hwang, S. Myeong, E. Lee, H. Jang, M. Yoon, H. Cha, J. Sung, M. G. Kim, D.-H. Seo, J. Cho, *Adv. Mater.* **2021**, *33*, 2100352.
- [29] M. Ångqvist, W. A. Muñoz, J. M. Rahm, E. Fransson, C. Durniak, P. Rozyczko, T. H. Rod, P. Erhart, *Adv. Theory Simul.* **2019**, *2*, 1900015.
- [30] C. J. Ballhausen, M. A. Weiner, *J. Electrochem. Soc.* **1963**, *110*, 97Cb.
- [31] D. A. Kitchaev, H. Peng, Y. Liu, J. Sun, J. P. Perdew, G. Ceder, *Phys. Rev. B* **2016**, *93*, 045132.
- [32] M. Saubanère, E. McCalla, J. M. Tarascon, M. L. Doublet, *Energy Environ. Sci.* **2016**, *9*, 984.
- [33] P. Yan, J. Zheng, Z.-K. Tang, A. Devaraj, G. Chen, K. Amine, J.-G. Zhang, L.-M. Liu, C. Wang, *Nat. Nanotechnol.* **2019**, *14*, 602.
- [34] W. Hua, S. Wang, M. Knapp, S. J. Leake, A. Senyshyn, C. Richter, M. Yavuz, J. R. Binder, C. P. Grey, H. Ehrenberg, S. Indris, B. Schwarz, *Nat. Commun.* **2019**, *10*, 5365.
- [35] X. Liu, G.-L. Xu, V. S. C. Kolluru, C. Zhao, Q. Li, X. Zhou, Y. Liu, L. Yin, Z. Zhuo, A. Daali, J.-J. Fan, W. Liu, Y. Ren, W. Xu, J. Deng, I. Hwang, D. Ren, X. Feng, C. Sun, L. Huang, T. Zhou, M. Du, Z. Chen, S.-G. Sun, M. K. Y. Chan, W. Yang, M. Ouyang, K. Amine, *Nat. Energy* **2022**, *7*, 808.
- [36] T. Liu, J. Liu, L. Li, L. Yu, J. Diao, T. Zhou, S. Li, A. Dai, W. Zhao, S. Xu, Y. Ren, L. Wang, T. Wu, R. Qi, Y. Xiao, J. Zheng, W. Cha, R. Harder, I. Robinson, J. Wen, J. Lu, F. Pan, K. Amine, *Nature* **2022**, *606*, 305.
- [37] R. A. House, J.-J. Marie, M. A. Pérez-Osorio, G. J. Rees, E. Boivin, P. G. Bruce, *Nat. Energy* **2021**, *6*, 781.
- [38] R. A. House, G. J. Rees, M. A. Pérez-Osorio, J.-J. Marie, E. Boivin, A. W. Robertson, A. Nag, M. Garcia-Fernandez, K.-J. Zhou, P. G. Bruce, *Nat. Energy* **2020**, *5*, 777.
- [39] J.-J. Marie, R. A. House, G. J. Rees, A. W. Robertson, M. Jenkins, J. Chen, S. Agrestini, M. Garcia-Fernandez, K.-J. Zhou, P. G. Bruce, *Nat. Mater.* **2024**. <https://doi.org/10.1038/s41563-024-01833-z>.
- [40] Z. Chen, J. Li, X. C. Zeng, *J. Am. Chem. Soc.* **2019**, *141*, 10751.
- [41] H. Chen, M. S. Islam, *Chem. Mater.* **2016**, *28*, 6656.
- [42] E. A. Raekelboom, A. L. Hector, J. Owen, G. Vitins, M. T. Weller, *Chem. Mater.* **2001**, *13*, 4618.
- [43] A. Tsuchimoto, X.-M. Shi, K. Kawai, B. Mortemard de Boisse, J. Kikkawa, D. Asakura, M. Okubo, A. Yamada, *Nat. Commun.* **2021**, *12*, 631.
- [44] X. Cao, H. Li, Y. Qiao, P. He, Y. Qian, X. Yue, M. Jia, J. Cabana, H. Zhou, *Joule* **2022**, *6*, 1290.
- [45] J. W. Essam, *Rep. Prog. Phys.* **1980**, *43*, 833.
- [46] M. B. Isichenko, *Rev. Mod. Phys.* **1992**, *64*, 961.
- [47] D. Stauffer, A. Aharony, *Introduction to Percolation Theory*, CRC Press, Boca Raton, FL **2018**.
- [48] A. Hunt, R. Ewing, B. Ghanbarian, *Percolation Theory for Flow in Porous Media*, Vol. 880, Springer, Berlin **2014**.
- [49] M. E. J. Newman, R. M. Ziff, *Phys. Rev. Lett.* **2000**, *85*, 4104.
- [50] P. N. Suding, R. M. Ziff, *Phys. Rev. E* **1999**, *60*, 275.
- [51] R. M. Ziff, H. Gu, *Phys. Rev. E* **2009**, *79*, 020102.
- [52] S. Sharifi-Asl, J. Lu, K. Amine, R. Shahbazian-Yassar, *Adv. Energy Mater.* **2019**, *9*, 1900551.
- [53] H. Zhang, H. Liu, L. F. J. Piper, M. S. Whittingham, G. Zhou, *Chem. Rev.* **2022**, *122*, 5641.
- [54] Y. Dong, J. Li, *Chem. Rev.* **2023**, *123*, 811.
- [55] G. Kresse, J. Hafner, *Phys. Rev. B* **1993**, *47*, 558.
- [56] G. Kresse, J. Furthmüller, *Phys. Rev. B* **1996**, *54*, 11169.
- [57] G. Kresse, J. Furthmüller, *Comput. Mater. Sci.* **1996**, *6*, 15.
- [58] P. E. Blöchl, *Phys. Rev. B* **1994**, *50*, 17953.
- [59] G. Kresse, D. Joubert, *Phys. Rev. B* **1999**, *59*, 1758.
- [60] J. P. Perdew, K. Burke, M. Ernzerhof, *Phys. Rev. Lett.* **1996**, *77*, 3865.
- [61] S. L. Dudarev, G. A. Botton, S. Y. Savrasov, C. J. Humphreys, A. P. Sutton, *Phys. Rev. B* **1998**, *57*, 1505.
- [62] V. I. Anisimov, J. Zaanen, O. K. Andersen, *Phys. Rev. B* **1991**, *44*, 943.
- [63] L. Wang, T. Maxisch, G. Ceder, *Chem. Mater.* **2007**, *19*, 543.
- [64] S. Grimme, J. Antony, S. Ehrlich, H. Krieg, *J. Chem. Phys.* **2010**, *132*, 154104.
- [65] G. Henkelman, B. P. Uberuaga, H. Jónsson, *J. Chem. Phys.* **2000**, *113*, 9901.
- [66] L. Wang, T. Maxisch, G. Ceder, *Phys. Rev. B* **2006**, *73*, 195107.